Biosensors and Bioelectronics 135 (2019) 22–29

Contents lists available at ScienceDirect

Biosensors and Bioelectronics

journal homepage: www.elsevier.com/locate/bios

Bimetallic cerium and ferric oxides nanoparticles embedded within mesoporous carbon matrix: Electrochemical immunosensor for sensitive detection of carbohydrate antigen 19-9

Minghua Wang, Mengyao Hu, Bin Hu, Chuanpan Guo, Yingpan Song, Qiaojuan Jia, Linghao He, Zhihong Zhang*, Shaoming Fang**

Henan Provincial Key Laboratory of Surface and Interface Science, Zhengzhou University of Light Industry, No. 136, Science Avenue, Zhengzhou, 450001, PR China

ARTICLE INFO

Keywords:
Cerium and ferric oxide nanoparticles
Mesoporous carbon
Bimetallic metal-organic frameworks
Electrochemical immunosensor
Detection of CA 19-9

ABSTRACT

A label-free electrochemical immunosensor was successfully developed for sensitively detecting carbohydrate antigen 19–9 (CA19-9) as a cancer marker. To achieve this, a series of bimetallic cerium and ferric oxide nanoparticles embedded within the mesoporous carbon matrix (represented by CeO_2/FeO_x@mC) was obtained from the bimetallic CeFe-based metal organic framework (CeFe-MOF) by calcination at different high temperatures. The formed CeO_2 or FeO_x nanoparticles were uniformly distributed within the highly graphitized mesoporous carbon matrix at the calcination temperature of 500 °C (represented by CeO_2/FeO_x@mC_{500}). However, the obtained nanoparticles were aggregated into large size when calcined at the temperatures of 700 and 900 °C. The CA 19–9 antibody can be anchored to the CeO_2/FeO_x@mC network through chemical absorption between carboxylic groups of antibody and CeO_2 or FeO_x by ester-like bridging. The CeO_2/FeO_x@mC_{500}-based immunosensor displayed superior sensing performance to the pristine CeFe-MOF, CeO_2/FeO_x@mC_{700}- and CeO_2/FeO_x@mC_{900}-based ones. Electrochemical impedance spectroscopy results showed that the developed immunosensor exhibited an extremely low detection limit of 10 $\mu U \cdot mL^{-1}$ (S/N = 3) within a wide range from 0.1 $mU \cdot mL^{-1}$ to 10 $U \cdot mL^{-1}$ toward CA 19–9. It also illustrated excellent specificity, good reproducibility and stability, and acceptable application analysis in the human serum solution which was diluted 100-fold with 0.01 M PBS solution (pH 7.4) and spiked with different amounts of CA19-9. Consequently, the proposed electrochemical immunosensor is capable enough of determining CA 19–9 in clinical diagnostics.

1. Introduction

Early diagnosis for cancers is extremely important in the treatment efficacy and quality of life of cancer patients. In china, pancreatic cancer is ninth most common malignant tumor (Li et al., 2007). Owning to the high degree of malignancy of the disease, the 5-year survival rate of pancreatic cancer patients is less than 5% (Hidalgo, 2010). Biomarkers secreted from tumor tissue, which can found in blood, tissue, and body fluids, are important diagnostic basis for clinic cancer. Carbohydrate antigen 19–9 (CA19-9), a kind a of carbohydrate antigen, is a glycoprotein highly associated with malignant tumors and shows great promise for malignant tumor detection, such as pancreatic cancer, colorectal cancer, liver cancer, gastric cancer, and ovarian cancer (Yang et al., 2015). The CA19-9 levels of normal healthy people are significantly lower than 37 $U \cdot mL^{-1}$ (Imaoka et al., 2016). Therefore, a slight elevation of CA19-9 level in blood means the possibility of the pancreatic cancer incidence and development (Humphris et al., 2012). Ultrasensitive detection of CA19-9 plays key roles in the early diagnosis, treatment, and prognosis of pancreatic cancer (Ludwig and Weinstein, 2005). At moment, several immunoassay approaches have been employed for detecting CA19-9 including electrochemical immunoassay (Zhu et al., 2016), chemiluminescent immunoassay (Lin et al., 2004), enzyme-linked immunosorbent assay (Parker et al., 1992) and radioimmunoassay (Ching and Rhodes, 1989). Despite of these efforts, these methods typically require labeling of the antibodies or antigens, leading to the assay process more complex, time consuming and expensive. Among different immunoassay methods, electrochemical label-free immunosensors have attracted increasing attention since they feature easy control, simple apparatus, and low-cost (Santharaman et al., 2016). Furthermore, aiming at designing and

* Corresponding author.
** Corresponding author.
E-mail addresses: 2006025@zzuli.edu.cn (Z. Zhang), mingfang@zzuli.edu.cn (S. Fang).

https://doi.org/10.1016/j.bios.2019.04.018
Received 21 February 2019; Received in revised form 5 April 2019; Accepted 9 April 2019
Available online 11 April 2019
0956-5663/

constructing highly sensitive electrochemical immunosensors, efficiently anchoring antibodies and producing amplified signals are the crucial steps (Sánchez et al., 2008). The sensitivity of the electrochemical immunosensors for the early detection of trace antigen depends on the adsorbing antibodies over the bioplatform, as well as the orientation of immobilized antibodies on the electrode surface (López-Alarcón and Denicola, 2013). Therefore, it is highly attractive to develop a novel nanomaterial-based bioplatform, which possesses good electrochemical and strong adsorption ability for antibodies.

Metal-organic frameworks (MOFs), known as coordination polymers or coordination networks, are a class of hybrid materials that consist of inorganic connectors and organic linker molecules (Zhou and Kitagawa, 2014). Owning to the specific features, including well-defined pore structure, large surface area, and specific functional sites that endows them with strong-bioaffinity toward biomolecules, have extended the application region of MOFs in various sensing fields (Li et al., 2015). The combined effects of the dynamics of analyte transport (within the MOF) and high loading capacity (due to a high volume-to surface-area ratio) can make contributions to the enhanced sensitivity of MOFs (Wang, 2017). For instance, Al-MOF (Liu et al., 2017a), Fe-MOF (Tang et al., 2018), Zr-MOF (Liu et al., 2017b), Cd-MOF (Kumar et al., 2016), Co-MOF (Xu et al., 2018a), Cu-MOF (Bhardwaj et al., 2017), and Zn-MOF (Wang et al., 2018a) have been employed as the scaffolds for immobilizing antibodies or other probes to detect various analytes. Additionally, recruiting the MOFs as precursors, recent work has presented a myriad of MOF-derived porous or hollow metal oxide nanostructures by thermal treatment (Zhang et al., 2017a), which has already found their applications in different fields (Mai et al., 2017). Regarding the porous structure and tailorable composition, the possibility of MOF-templated metal oxides as an alternative to extract biomolecules instead of MOFs have been evaluated. In the past decade, various metal oxides, such as CuO, ZnO, NiO, Co_3O_4, and Fe_2O_3, were synthesized by calcining their corresponding MOFs (Zou and Li, 2018). Because of their large specific surface area, superior electrochemical performance, and excellent biocompatibility, the derivatives from MOFs have been paid more attention to be employed as the substrate to construct electrochemical biosensors for trace detection of different analytes (Dang et al., 2017). Nevertheless, most of metal oxides derived from MOFs were exploited as the non-enzyme electrocatalysts for detecting small biomolecules (Zhang et al., 2016a). Rare reports have been observed about their applications in immunosensors or immunosensor fields for detecting the cancer markers. For instance, Fe_3O_4@mC nanocomposite derived from Fe-MOF was applied as the scaffold for immunosensor for sensitively detecting oxytetracycline, giving a low limit of detection (LOD) of 0.027 pg mL^{-1} (Song et al., 2017). NiO_xFeO_y@mC derived from the hollow NiFe Prussian blue analogue was used as the scaffold for sensitively detecting adenosine triphosphate, showing a LOD of 0.98 fg mL^{-1} (Wang et al., 2018b).

Bimetallic nanoparticles composed of two different metal elements have also received wide spread attention especially in the field of electrochemical immunoassays. They often show improved sensing performance than their monometallic counterparts due to the synergistic effect and the electronic effect (Yang et al., 2017a). Among different MOFs, a mixed valence state of Ce-MOF and Fe-MOF possessed an excellent mimics of catalytic activity, hence showing a sensitive electrochemical approach for the detection of small biomolecules (Peng et al., 2018). Especially, CeO_2 as a typical rare earth oxide has attracted extensive attention due to the special 4f electronic structure, along with the excellent electrochemical performance, chemical inertness, non-toxicity, and negligible swelling (Kašpar et al., 1999). A wide scope to explore the electrochemical properties of the CeO_2-based nanocomposite for biosensor application and biomarker detection has been found. CeO_2-reduced graphene oxide nanocomposite was explored to be as the immunosensor for detecting the cancer marker, Cyfra-21-1 (Pachauri et al., 2018). CuMn-CeO_2 was developed as redox probe, signal amplifier and matrix for sensitive detection of procalcitonin since CeO_2 possesses special surface mixed-valence properties (Yang et al., 2017a). Au nanoparticles were used to combine anti-PSA1 (Ab1) to CeO_2 via the Au-NH_2 covalent bond and meanwhile to enhance the sensitivity of the immunosensor (Zhao et al., 2016). GO/MWCNTs-COOH/Au@CeO_2 was served as the sensing platform for detecting carcinoembryonic antigen, giving a LOD of 0.02 ng mL^{-1} (Pang et al., 2015). Fe_2O_3@C composite was synthesized by annealing of Fe-MOFs. The Fe_2O_3@C-based biosensor exhibited wide linear range and the low LODs for the determination of H_2O_2 and paraoxon (Wei et al., 2018). Antibody against CA19-9 was covalently immobilized on the magnetized carbon nanotubes (Fe_3O_4-MCNTs) and was employed to capture CA19-9 in blood with LOD of 30 U·mL^{-1} (Huang et al., 2017). At moment, however, no report was observed for the application of CeO_2/FeO_x hybrid as the immunosensor for detecting CA19-9.

In our previous work, cerium and cupric oxide nanoparticles embedded within the mesoporous carbon matrix were obtained by the calcination of bimetallic CeCu-MOF in N_2 atmosphere (CeO_2/CuO_x@mC) (Wang et al., 2019). The CeO_2/CuO_x@mC-based aptasensor was fabricated for the tobramycin detection, giving an extremely low LOD of 2.0 fg mL^{-1} within a broad linear range from 0.01 pg mL^{-1} to 10 ng mg L^{-1}. However, the optimized bioplatform of aptasensor, CeO_2/CuO_x@mC calcined at 900 °C, exhibited the favorable aggregation behavior, showing the uneven surface morphology. As such, it would be very desirable to develop a novel bimetallic oxides composed of cerium for the biosensor fabrication at a relatively low calcination temperature. Considering the advantages of CeO_2 and FeO_x in the sensing fields, we designed and prepared a novel bimetallic CeFe-MOF, following by pyrolyzing it to form a series of structure-controlled mixed CeFe oxides under different high temperatures (500, 700, and 900 °C), which was embedded within the mesoporous carbon matrix (represented by CeO_2/FeO_x@mC) for the first time. Subsequently, the series of CeO_2/FeO_x@mC were employed as new scaffolds for binding the CA19-9 antibody to sensitively detect CA19-9 (Scheme 1). As compared with the routine immunosensors for detecting CA19-9, the constructed CeO_2/FeO_x@mC-based electrochemical immunosensor displayed the superior sensing performances. It is mainly attributed to the following reasons: (i) antibody molecules can be adsorbed on CeO_2 through chemical absorption between carboxylic groups of antibody and CeO_2 by ester-like bridging (Yang et al., 2017b); (ii) Fe_2O_3 can improve electrochemical properties of the transducers and strengthen the conjugation with biological compounds (Wei et al., 2018); (iii) the formed graphitized carbon layer with porous structure and high specific surface area was also implemented as the matrix to provide interface with abundant sites for antibody immobilization (Wang and Dai, 2015). After blocking with BSA and incubation of target CA19-9, the electrochemical response signal variation can be detected owing to the antigen-antibody reaction (Sha et al., 2015). Therefore, it would be extremely expectant to construct a novel electrochemical immunosensor based on CeO_2/FeO_x@mC for early detecting cancer markers and further find the possible applications in early cancer diagnosis.

2. Experimental section

The detailed description of reagents and materials, preparation of solutions, characterizations, and pretreatment of the bare Au electrode (AE) were supplied in the part of "**S1. Experimental section**" in the Supporting Information (SI).

2.1. Preparation of the Ce-MOF, CeO_2@mC_{500}, CeFe-MOF, and series of CeO_2/FeO_x@mC nanocomposites

The CeFe-MOF was synthesized following the procedure reported by Yu et al., (2018) with slight modifications. Typically, $Ce(NO_3)_3{\cdot}6H_2O$ (1.0 mmol) and $Fe(NO_3)_3{\cdot}3H_2O$ (1.0 mmol) were dissolved in an ethanol/water (v/v = 1/1, 30 mL) system to obtain Solution **A**. 1,3,5-Benzenetricarboxylic acid (H_3BTC) (3.0 mmol) was also dissolved in an

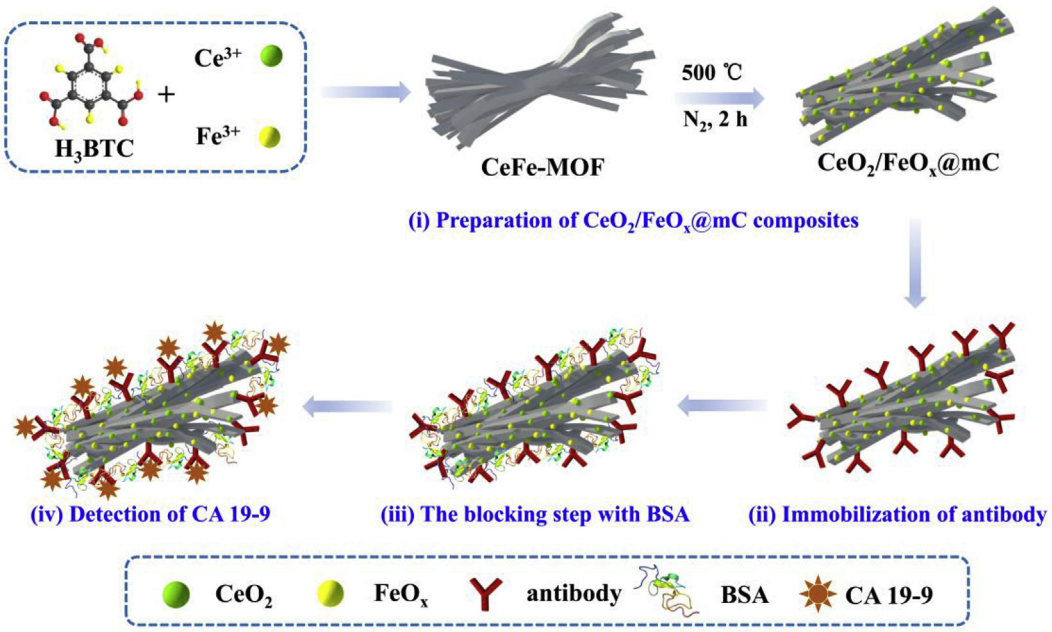

Scheme 1. The schematic diagram of the immunosensor fabrication based on CeO_2/FeO_x@mC for detecting CA19-9, including (i) the preparation of the series of CeO_2/FeO_x@mC composites, (ii) the adsorption of the CA19-9 antibody, (iii) the blocking step with BSA, and (iv) the detection of CA19-9.

ethanol/water (v/v = 1/1, 70 mL) mixture to form Solution **B**. Then, Solution **A** was poured slowly into Solution **B** under stirring. The pink precipitate appeared after the mixture remained aged for 24 h. The product was washed with an equal amount of ethanol/water mixture several times, and then dried in an oven at 60 °C. The resultant sample was referred to as the CeFe-MOF. Subsequently, the CeFe-MOF was calcined in a tube furnace at different temperatures, i.e., 500, 700, and 900 °C, with a heating rate of 2 °C·min^{-1} and maintained for 2 h in N_2 atmosphere, individually. After natural cooling to room temperature, different kinds of black CeO_2/FeO_x@mC powder were obtained and denoted as $CeO_2/FeO_x@mC_{500}$, $CeO_2/FeO_x@mC_{700}$, and $CeO_2/FeO_x@mC_{900}$ in according to the calcination temperature.

For comparison, the Ce-MOF was prepared by the same way with that of the CeFe-MOF without the use of $Fe(NO_3)_3{\cdot}3H_2O$. The $CeO_2@mC_{500}$ was obtained by calcination of the Ce-MOF at 500 °C using the same conditions with the $CeO_2/FeO_x@mC_{500}$ composite. Additionally, the structure component and surface morphology analysis of the Ce-MOF and $CeO_2@mC_{500}$ composite were supplied in the part of **S2** (See the Supporting Information).

2.2. Fabrication of Ce-MOF-, $CeO_2@mC_{500}$-, CeFe-MOF-, and series of the CeO_2/FeO_x@mC-based immunosensors

For preparation of suspension of $CeO_2/FeO_x@mC_{500}$, 1 mg $CeO_2/FeO_x@mC_{500}$ powder was added to 1 mL of Milli-Q ultrapure water and sonicated thoroughly for 40 min until a homogeneous suspension was obtained. Similarly, the suspension of Ce-MOF, $CeO_2@mC_{500}$, CeFe-MOF, $CeO_2/FeO_x@mC_{700}$, and $CeO_2/FeO_x@mC_{900}$ were prepared in the same way. Taking the fabrication of the $CeO_2/FeO_x@mC_{500}$-based immunosensor as the example, it was prepared as the following procedures. Firstly, 10 μL of $CeO_2/FeO_x@mC_{500}$ suspension was dropped onto the pre-treated AE and dried at the room temperature for 6 h (represented as the $CeO_2/FeO_x@mC_{500}$/AE). Subsequently, the $CeO_2/FeO_x@mC_{500}$/AE was immersed into the CA19-9 antibody solution (1.0 μg·mL^{-1}) for 4 h, and washed with phosphate buffered saline (PBS, pH 7.4) thoroughly (represented as the Ab/$CeO_2/FeO_x@mC_{500}$/AE). For comparison, the Ce-MOF-, $CeO_2@mC_{500}$, CeFe-MOF-, $CeO_2/FeO_x@mC_{700}$- and $CeO_2/FeO_x@mC_{900}$-based immunosensors were developed in the same way. All obtained electrochemical immunosensors were used for further measured and stored in the refrigerator (4 °C) when not use.

2.3. Electrochemical measurements

All electrochemical measurements were carried out on CHI760E electrochemical workstation (Chenhua, Shanghai, China), equipped with a common three-electrode system. Modified AE, Pt wire, and Ag/AgCl (saturated KCl) served as working electrode, counter electrode and reference electrode, respectively. The cyclic voltammetry (CV) was performed from −0.2 V to 0.8 V at the scan rate of 100 mV s^{-1} in 5 mM $K_3[Fe(CN)_6]/K_4[Fe(CN)_6]$ (1:1) mixture as a redox probe in 0.01 M PBS (pH 7.4, containing 0.14 M NaCl and 0.1 M KCl). Electrochemical impedance spectra (EIS) were recorded within the frequency range of 0.01 Hz–100 kHz with amplitude of 5 mV. The EIS spectra were analyzed using ZView2 software. The equivalent circuit (Fig. S1) is consisted of solution resistance (R_s), charge-transfer resistance (R_{ct}), constant-phase element (*CPE*), and Warburg impedance (*W*). The detailed electrochemical experiments of the proposed immunosensors for detecting CA19-9 were described in **S1.6**.

3. Results and discussion

3.1. Crystal and chemical structure of the CeFe-MOF and the series of CeO_2/FeO_x@mC composites

The crystal and chemical structure of the CeFe-MOF and the series of CeO_2/FeO_x@mC composites were characterized by powder X-ray diffraction measurements (PXRD), Raman spectra, Fourier transform infrared spectroscopy (FT-IR) and X-ray photoelectron spectroscopy (XPS) (Fig. S4) and analyzed in detail in the part of **S3** (See the Supporting Information). Briefly, the XRD pattern of bimetallic CeFe-MOF shows main diffraction peaks of the Ce-MOF, indicating the preferential orientation of Ce-MOF. In terms of $CeO_2/FeO_x@mC_{500}$ composite, the characteristic diffraction peaks of face-centered cubic CeO_2 and α-Fe_2O_3 were coexisted, hinting that the Ce and Fe coordination centers were transferred into its corresponding metal oxides. When the calcination temperature increased to 700 and 900 °C, and the narrower peak width with high intensity was obtained, displaying their high

crystallinity of metal oxides. Additionally, the diffraction peaks of Fe_3O_4 and metallic state Fe crystals also appeared in the CeO_2/FeO_x@mC_{900} composite. The Raman spectra of the CeFe-MOF before and after the pyrolysis gave the helpful information about the chemical structure change during the calcination. The appearance of typical D and G bands at 1335 cm^{-1} and 1595 cm^{-1} in the series of CeO_2/FeO_x@mC hints the formation of porous carbon with disordered and graphitic structures. Compared with the I_G/I_D ratios of CeO_2/FeO_x@mC_{700} (1.01) and CeO_2/FeO_x@mC_{900} (0.93) composites, a higher I_G/I_D ratio (1.21) of the CeO_2/FeO_x@mC_{500} reveals its high content of graphitized carbon. The formation of graphitized carbon can not only improve the electrical conductivity but also enhance the durability of the material (Li et al., 2016). In comparison with the CeFe-MOF, the decline in the FT-IR spectrum intensity of COO- group containing in the series of the CeO_2/FeO_x@mC composites illustrate the thermal decomposition of the organic ligands. Moreover, the enhancement of the FT-IR spectrum intensity of the band at 550 cm^{-1} originated from Ce-O stretching indicates the formation of the metal oxide, consistent with the PXRD results.

To further investigate the chemical structures and surface components of CeFe-MOF and CeO_2/FeO_x@mC composites, XPS analysis was performed. As summarized in Fig. S4d and Table S1, the peaks at 284.6 and 531.4 eV are characteristic of C 1*s* and O 1*s*, while the peaks in regions of 705–730 eV and 880–920 eV are characteristic of Fe 2*p* and Ce 3*d*, respectively. As for the CeFe-MOF, the Ce 3*d* spectrum (Fig. S5a) presents two main peaks labeled as *v′* (885.1 eV) and *u′* (903.9 eV), which are correspond to Ce(III) states; while the other four peaks of *v* (881.8 eV), *v″* (886.9 eV), *u* (900.2 eV) and *u″* (907.1 eV), are characteristic peaks of Ce(IV). In terms of the series of CeO_2/FeO_x@mC composites (Fig. 1a1, 1b1 and 1c1), the peaks of v_0, *v′*, u_0 and *u′* are attributed to Ce(III); while *v*, *v″*, *v‴*, *u*, *u″* and *u‴* are assigned to Ce(IV) (Zhang et al., 2004). According to the ratio of Ce(IV) related peak areas to the sum of the integrated peak areas of Ce 3*d*, the calculated content of Ce(IV) containing in the CeO_2/FeO_x@mC composites increases in comparison with the pristine CeFe-MOF due to the formation of CeO_2 crystals during the pyrolysis process. With regard to the Fe 2*p* XPS spectra (Fig. S5b and Fig. 1a2, 1b2 and 1c2) of all samples, the peaks at binding energies of 710.5 and 719.6 eV are characteristic peaks of Fe (II), whereas the peaks at 712.6 and 721.6 eV are ascribed to Fe(III). The peaks at 715.8 and 717.8, and 724.5 eV are due to the satellite peaks for Fe $2p_{3/2}$ and Fe $2p_{1/2}$, respectively. The high-resolution C 1*s* XPS spectra of the CeFe-MOF (Fig. S5c) and CeO_2/FeO_x@mC composites (Fig. S6) show four peaks at 284.6, 285.4, 288.5, and 290.9 eV, corresponding to C=C/C-C/C-H, C-O, O=C-O groups, and π-π* bonds, respectively. However, the peak related to O=C-O groups obviously is weakened in the series of CeO_2/FeO_x@mC samples, which is caused by the pyrolysis of the CeFe-MOF under high temperature. As illustrated in Fig. S5d, the high-resolution O 1*s* XPS spectrum of CeFe-MOF can be fitted into three oxygen species including C=O (530.6 eV), C-O (531.9 eV), and adsorbed O (533.0 eV). However, an additional peak at 529.6 eV was observed for the series of CeO_2/FeO_x@mC composites (Fig. 1a3, 1b3, and 1c3), which is attributed to Ce-O or Fe-O bonds. These results imply that the formation of metal oxides, which is consistent with the PXRD and FT-IR results, along with the presence of different valence states of Ce and Fe after the calcination under high temperature.

3.2. Surface morphologies of all samples

Scanning electron microscope (SEM) and transmission electron microscopy (TEM) images of the CeFe-MOF shows its rod-like shape with diameters of around 100 nm and lengths of several micrometers. The rods exhibit rough surface and easily aggregate into bundles (Fig. S7). After the calcination at 500 °C, the formed CeO_2/FeO_x@mC_{500} displays a rather rough surface (Figs. S8a and S8b). A large amount of nanoparticles are uniformly grown over the nanorods surface. With the

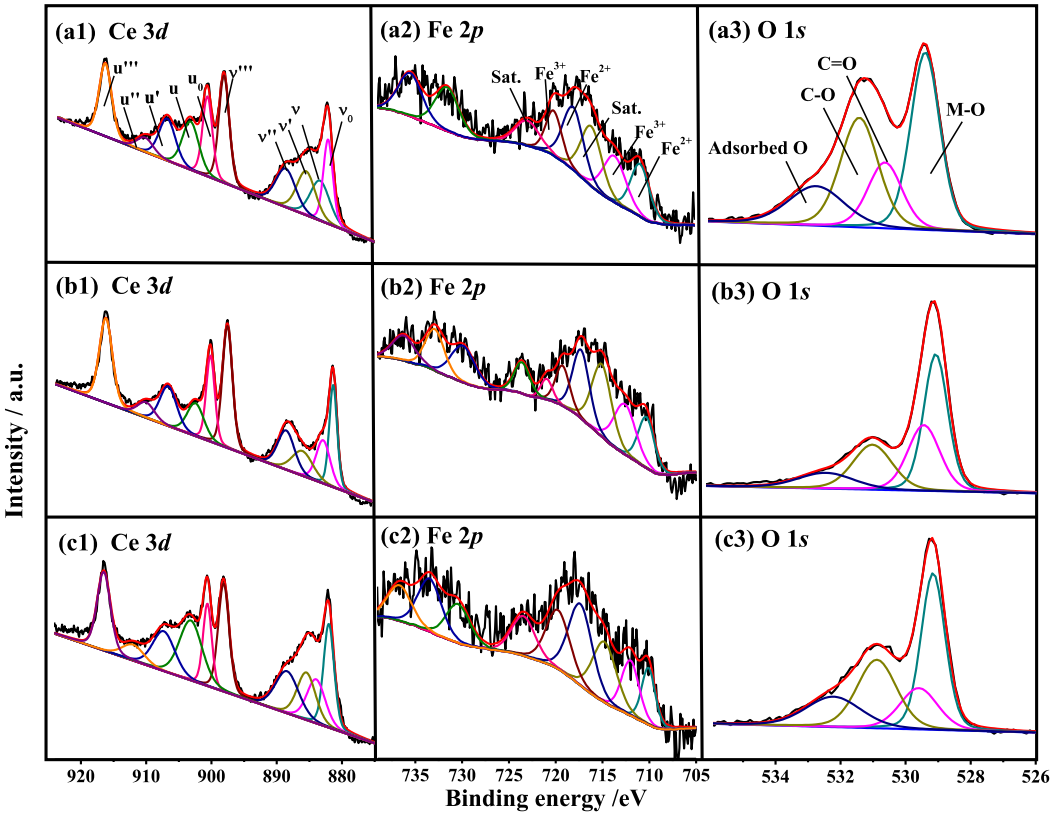

Fig. 1. High-resolution Ce 3*d*, Fe 2*p*, and O 1*s* XPS spectra of the (a) CeO_2/FeO_x@mC_{500}, (b) CeO_2/FeO_x@mC_{700}, and (c) CeO_2/FeO_x@mC_{900} composites.

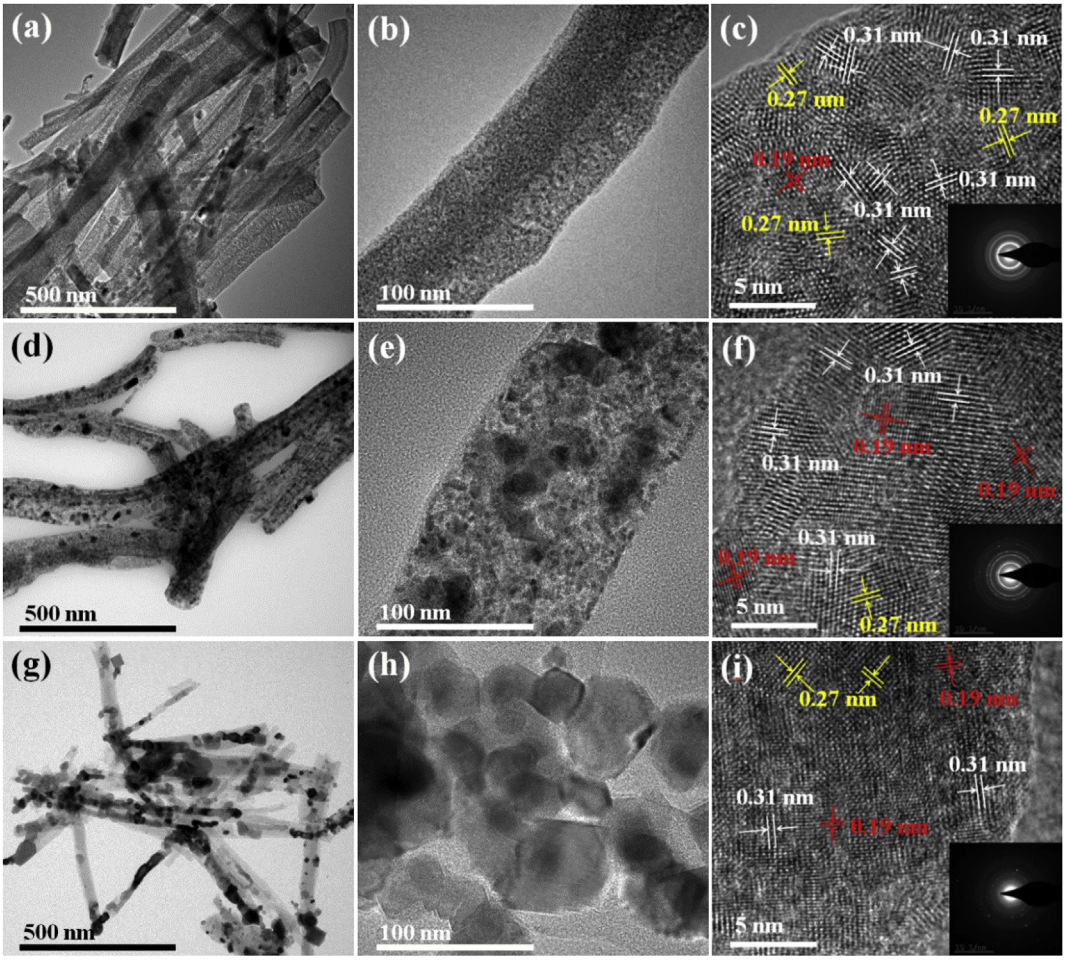

Fig. 2. TEM and HR-TEM images of (a, b, c) $CeO_2/FeO_x@mC_{500}$, (d, e, f) $CeO_2/FeO_x@mC_{700}$, and (g, h, i) $CeO_2/FeO_x@mC_{900}$ composites. The insets in (c), (f), and (i) are the corresponding selected area electron diffraction (SAED) patterns.

calcination temperature increasing, the nanoparticles are prone to aggregate into one with big size (Fig. S8c-f). The TEM and high-resolution TEM (HR-TEM) images of $CeO_2/FeO_x@mC_{500}$ reveal that the nanorods demonstrate loose and porous structure decorated with many small nanoparticles (Fig. 2a and b), which are not only directly attached to surface but also embedded within the formed carbon rods. By contrast, large nanocrystals with irregular shape are observed in the TEM images of $CeO_2/FeO_x@mC_{700}$ (Fig. 2d and e) and $CeO_2/FeO_x@mC_{900}$ composites (Fig. 2g and h). As shown in Fig. 2c, f, and 2i, the interlayer spacings are measured to be 0.31 nm and 0.19 nm, which are indexed to the (111) and (220) crystal planes of the cubic CeO_2, respectively, while the lattice fringes of 0.27 nm could be indexed to the (104) plane of Fe_2O_3 (Lv et al., 2016) and/or the (200) plane of CeO_2 (Zhang et al., 2018). The scattered diffraction pattern and rings are shown in the selected area electron diffraction (SAED) analysis (insets of Fig. 2c, f and 2i), indicating that the metal oxides are polycrystalline structure, consistent with the results of PXRD, FT-IR, and XPS characterizations. In summary, the metallic coordination centers containing in MOFs can be transferred into their corresponding metal oxides, while the organic ligands are changed to the mesoporous carbon during the calcination procedure. Additionally, the large surface area and well-defined nanostructures of parent MOFs can be preserved. The similar results were also reported for other MOFs-derived composites, such as NiCo@$NiCoO_2$ core@shell nanoparticles fabricated by the reductive carbonization of bimetallic NiCo-MOF microrod arrays (Xu et al., 2018b), Cu/Cu_2O@C core–shell nanocomposite monodispersed on the surface of reduced graphene oxide by calcination of Cu-MOFs/graphene oxide composite structure (Yang et al., 2018), multimetal oxides derived from integrated multiple-metal MOFs (Castillo-Blas et al., 2019). However, most of these MOFs-derivatives were applied as catalysts for clean energy (Cheng et al., 2018) or energy conversion (Yang and Wang, 2018). It is still in the early stage for the exploration of these nanomaterials in the biosensing fields (Lei and Ju, 2012).

3.3. Electrochemical characterization of the developed immunosensors

CV technique was utilized to determine the fabrication procedure of the immunosensor, in which $[Fe(CN)_6]^{3-}/[Fe(CN)_6]^{4-}$ was used as the redox probe (see a detailed discussion in **S5** and Fig. S9). The results indicate that biomolecules were assembled on the sensing layer and hinder the diffusion of ferricyanide toward the electrode surface. Additionally, the variation in each step of the electrode behavior after the modification with the as-prepared nanomaterials, antibody adsorption and CA19-9 binding was efficiently detected by EIS technique. The semicircle diameter in the impedance spectra equals the electron transfer resistance (R_{ct}). As for the CeFe-MOF-based immunosensor toward CA19-9 (Fig. S10a), the R_{ct} values of AE, CeFe-MOF/AE, Ab/CeFe-MOF/AE, BSA/Ab/CeFe-MOF/AE, and CA19-9/BSA/Ab/CeFe-MOF/AE are 0.10, 0.42, 0.56, 0.62, and 0.71 kΩ, which increases continuously at each step. As shown in Fig. 3a, the bare AE shows a small semicircle with a R_{ct} value of 0.09 kΩ (curve *i*), suggesting a low transfer resistance. After the modification with the $CeO_2/FeO_x@mC_{500}$ composite, the R_{ct} value of the modified electrode increases to 0.51 kΩ (curve *ii*), which is mainly owing to the $CeO_2/FeO_x@mC_{500}$ film hinders the electron exchange between the redox probe and the electrode. Subsequently, the R_{ct} value of Ab/$CeO_2/FeO_x@mC_{500}$/AE further

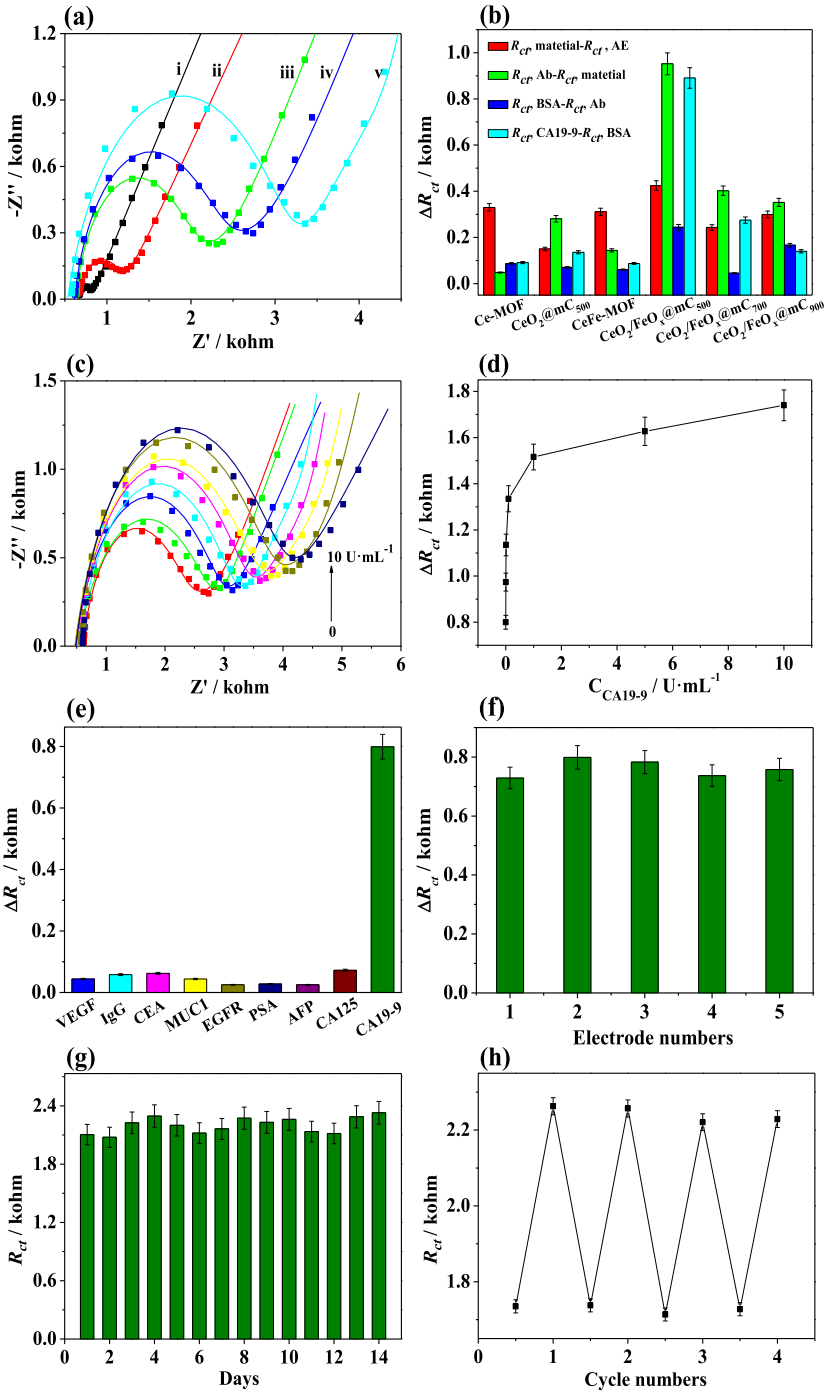

Fig. 3. (a) Nyquist diagrams of CeO_2/FeO_x@mC_{500} modified electrode in PBS (0.01 M, pH 7.4) containing 5 mM $Fe(CN)_6^{3-/4-}$: (i) bare AE; (ii) CeO_2/FeO_x@mC_{500}/AE; (iii) Ab/CeO_2/FeO_x@mC_{500}/AE; (iv) Ab/CeO_2/FeO_x@mC_{500}/AE blocked with 0.01 ng mL^{-1} BSA and (v) the proposed immunosensor incubated with 0.01 U·mL^{-1} CA19-9. (b) Differences in ΔR_{ct} values at each stage for the detection of CA19-9 using the Ce-MOF-, CeO_2@mC_{500}-, CeFe-MOF-, CeO_2/FeO_x@mC_{500}-, CeO_2/FeO_x@mC_{700}-, and CeO_2/FeO_x@mC_{900}-based immunosensors. (c) EIS responses of the CeO_2/FeO_x@mC_{500}-based immunosensor with different CA19-9 concentrations (0, 0.0001, 0.001, 0.01, 0.1, 1.0, 5.0 and 10 U·mL^{-1}). (d) Dependence of ΔR_{ct} on the concentration of CA19-9. Inset: calibration curve for CA19-9 determination. (e) Specificity, (f) reproducibility, (g) stability, and (h) regenerability of the CeO_2/FeO_x@mC_{500}-based immunosensor for detecting of 0.0001 U·mL^{-1} CA19-9. The error bars represented average standard errors for three measurements (n = 3).

increases to 1.46 kΩ (curve *iii*), implying that antibody is immobilized over the CeO_2/FeO_x@mC_{500} layer and blocked the electron transfer in the electrochemical probe (Yang et al., 2015). When the Ab/CeO_2/FeO_x@mC_{500}/AE layer was blocked with BSA to remove the non-specific adsorption between the nanocomposite surface and analyte molecule, a larger semicircle with R_{ct} value of 1.71 kΩ was observed (curve *iv*) due to the steric hindrance. When the incubation time of CA19-9 increased, the R_{ct} value at BSA/Ab/CeO_2/FeO_x@mC_{500}/AE gradually raised and leveled off (Fig. S11), indicating that the absorption process can balance within 80 min. Therefore, the incubation time of 2 h was chosen for further electrochemical measurements. After incubation of CA19-9 solution (0.01 U·mL^{-1}), the R_{ct} value increases to 2.60 kΩ (curve *v*), implying that the target antigen molecules were captured and attached to the surface of the modified electrode through antigen-antibody reaction (Sha et al., 2015). For comparison, the Nyquist diagrams of the CeO_2/FeO_x@mC_{700}, CeO_2/FeO_x@mC_{900}, Ce-MOF, CeO_2@mC_{500} toward CA19-9 were also performed at the same conditions (Figs. S10b–e). Although the same determination behaviors are obtained, the different immunosensors exhibit different R_{ct} values (Table S2).

On the account that the variation in the R_{ct} ($\Delta R_{ct} = R_{ct,\,i+1} - R_{ct,\,i}$) value can represent the surface coverage and adsorbed layer amount (Sheikhzadeh et al., 2016), the ΔR_{ct} values of each step for CA19-9 detection are calculated and summarized in Fig. 3b to compare the detection sensitivities of six kinds of immunosensors based on Ce-MOF, CeO_2@mC_{500}, CeFe-MOF, CeO_2/FeO_x@mC_{500}, CeO_2/FeO_x@mC_{700}, and CeO_2/FeO_x@mC_{900}. By comparison with Ce-MOF, the formed CeO_2@mC_{500} shows not only good conductivity but also a higher ΔR_{ct} value,

indicating more adsorption amount of antibody molecules on the surface of CeO_2@mC_{500} layer. Moreover, after binding with the antibody, the caused ΔR_{ct} value of CeFe-MOF/AE (0.14 kΩ) is higher than that of Ce-MOF/AE (0.05 kΩ). It suggests the synergistic effect between Ce and Fe in the bimetallic MOF for biomolecular immobilization. The ΔR_{ct} values ($R_{ct,\ Ab}$ - $R_{ct,\ material}$) of series of CeO_2/FeO_x@mC composites are distinct differences and followed the order: CeO_2/FeO_x@mC_{500} (0.95 kΩ) > CeO_2/FeO_x@mC_{700} (0.40 kΩ) > CeO_2/FeO_x@mC_{900} (0.35 kΩ). When calcinated under 500 °C, the formed CeO_2/FeO_x@mC_{500} has a nanostructure with uniform distribution of CeO_2/FeO_x nanoparticles embedded within graphitized mesoporous carbon matrix and special functional groups, which can provide interface with abundant sites (Wang and Dai, 2015) and is in favor of immobilizing the antibody molecules through ester-like bridging (Yang et al., 2017b). Accordingly, a large amount of antibody molecules can be immobilized on CeO_2/FeO_x@mC_{500} nanocomposite in comparison with CeO_2/FeO_x@mC_{700} and CeO_2/FeO_x@mC_{900}. Since more target protein CA19-9 can assemble on the CeO_2/FeO_x@mC_{500}-based immunosensor, a much higher R_{ct} value is observed compared with those of CeO_2/FeO_x@mC_{700}, CeO_2/FeO_x@mC_{900}, and pristine CeFe-MOF. The result indicates that the CeO_2/FeO_x@mC_{500} sensing layer is expected to be an outstanding platform for efficiently detecting CA19-9.

3.4. Detection of CA19-9 using the CeO_2/FeO_x@mC_{500}-based immunosensor

To assess the analytical performance of the CeO_2/FeO_x@mC_{500}-based immunosensor, a series of CA19-9 standard solutions with different concentrations were analyzed by EIS technique. As shown in Fig. 3c, the diameters of semicircle of the electrochemical sensor increase with increasing the CA19-9 concentration. It demonstrated that the ΔR_{ct} values of the immunosensor ($\Delta R_{ct} = R_{ct,\ CA19\text{-}9}$ - $R_{ct,\ antibody}$) increase with the concentrations of CA19-9 within the range from 0.1 $mU{\cdot}mL^{-1}$ to 10 $U{\cdot}mL^{-1}$. Thus, the detection behavior of CA 19–9 was obeyed to the Langmuir-Freundlich isotherm, which seems a typical behavior for antigen-antibody adsorption in immunosensors (Thapa et al., 2017). The LOD was calculated by the IUPAC method:

$$\mathrm{LOD} = \frac{3S_b}{m}$$

where S_b refers to standard deviation of the blank (signal before incubation of target CA19-9) and m is the slope, which refers to the gradient of the calibration graph. The LOD was calculated graphically from the calibration curve in Fig. 3d by considering the steep slope encompassing the first four data points. The LOD can be obtained to be 10 $\mu U{\cdot}mL^{-1}$. Consequently, due to the high sensitivity, the electrochemical immunosensor can be used to detect the trace CA19-9 in the early diagnosis of cancer. Compared with the listed noble metal- and carbon material-based CA19-9 immunoassays (Table 1), the proposed CeO_2/FeO_x@mC_{500}-based immunosensor exhibits superior sensitivity and a low LOD for detection of CA19-9. These can be ascribed to the following reasons: (i) specific cavities and open channels were reserved by pyrolysis of CeFe-MOF under controllable conditions, which can provide pathways for electron transfer and reactant species diffusions; (ii) owing to the synergistic effect between bimetallic Ce and Fe elements, the as-synthesized CeO_2/FeO_x@mC with functional-rich chemical groups is favorable for biomolecules absorption and can amplify the electrochemical signal of the immunosensor; (iii) the formed graphitized porous carbon structure uniformly embedded with CeO_2/FeO_x nanocrystals also provide abundant binding sites for antibody molecules immobilization, leading to specific recognition and sensitive detection of target antigen molecules.

3.5. Specificity, reproducibility, stability, and regenerability of the developed immunosensor

To evaluate the specificity of the CeO_2/FeO_x@mC_{500}-based immunosensor, the influence of some representative interfering proteins, including vascular endothelial growth factor (VEGF), immunoglobulin G (IgG), carcinoembryonic antigen (CEA), mucin 1 (MUC1), epidermal growth factor receptor (EGFR), porcine serum albumin (PSA), alpha-fetoprotein (AFP) and carbohydrate antigen 125 (CA125) with concentration of 0.01 $ng\ mL^{-1}$, was studied in the presence of 0.1 $mU{\cdot}mL^{-1}$ CA19-9. As illustrated in Fig. 3e, no remarkable ΔR_{ct} value is observed in the interfering solution as compared to the result obtained signal change in the CA19-9 solution. It demonstrates that the proposed immunosensor performs a high specificity for CA19-9 detection owing to the specific recognition between the antibody and CA19-9 (Weng et al., 2017). The reproducibility of the immunosensor was verified by detecting 0.1 $mU{\cdot}mL^{-1}$ CA19-9 with five same immunosensors that was prepared independently. The relative standard deviation (RSD) of 3.74% is obtained (Fig. 3f), indicating good reproducibility of the proposed immunosensor. Moreover, in order to assess the storage stability of the CeO_2/FeO_x@mC_{500}-based immunosensor, the immunosensor was stored at 4 °C and measured once a day. It can be seen from Fig. 3g that the R_{ct} response to the same concentration of CA19-9 exhibits a relatively small change (RSD = 3.72%) after a long storage time of two weeks, hinting the immunosensor possesses acceptable stability. Additionally, the immunosensor was regenerated by being soaked in 1 M H_2SO_4 solution for 20 min and washed thoroughly with 0.01 M PBS (pH 7.4). Following, EIS measurements were performed and the procedure was repeated continuously. As shown in Fig. 3h, the repeatable R_{ct} response signal to the CA19-9 solution can be observed, demonstrating the regenerability of the proposed immunosensor is also good.

3.6. Application of the proposed immunosensor

The proposed CeO_2/FeO_x@mC_{500}-based immunoassay was employed to detect different CA19-9 concentrations diluted in human serum samples. Certain concentrations of CA19-9 were added into 100-fold dilution of the human serum with 0.01 M PBS solution (pH 7.4) and the EIS plots were recorded. The concentrations of CA19-9 were

Table 1
Comparison between the proposed assay and other method for detection of CA19-9.

Materials	Analytical technique	Linear range ($U{\cdot}mL^{-1}$)	LOD ($U{\cdot}mL^{-1}$)	Refs.
Antibody–AuNP–G-quadruplex/hemin	Chemiluminescent immunoassays	0.025–1.00	0.016	Shi et al. (2014)
AuPt nanocalliandras	Differential pulse voltammetry	0.05–50	0.03	Weng et al. (2017)
Cuboid silver modified paper working electrode	Square wave voltammetry	0.1–100	0.00004	Li et al. (2014)
Au@Pd-Gra/Thi-Ab2/HRP bioconjugate	DPV	0.015–150	0.006	Yang et al. (2015)
Multi-functionalized graphene oxide	Electrochemiluminescence (ECL)	0.001–5	0.0005	Sha et al. (2015)
Ag@BSA-luminol	ECL	0.0005–150	0.0002	Zhang et al. (2016b)
TiO_2NWs/Au/CdSe@ZnS	Photoelectrochemical immunoassay	0.01–200	0.0039	Zhu et al. (2016)
MWCNT-Pt-luminol nanocomposite	ECL	0.0001–10	0.000046	Zhang et al. (2017b)
Carbon quantum dots/gold nanocomposite	Fluorescence immunoassay	0.01–350	0.007	Alarfaj et al. (2018)
CeO_2/FeO_x@mC_{500}	EIS	0.0001–10	0.00001	**this work**

calculated by using BSA/Ab/CeO_2/FeO_x@mC_{500}/AE assay according to the proposed method. As summarized in Table S3, the recoveries range from 95.2 to 106.4% and RSD values are less than 2% for CA19-9 determination, indicating the desirable practicality of the immunosensor. Therefore, the proposed CeO_2/FeO_x@mC-based electrochemical immunosensor has promising potential applications in cancer markers detection and early diagnosis.

4. Conclusions

In summary, a label-free electrochemical immunosensor based on the bimetallic CeFe-MOF-derived CeO_2/FeO_x@mC nanocomposite for the ultrasensitive detection of CA19-9 was developed. The calcination temperature used in the CeO_2/FeO_x@mC nanocomposite preparation has played an important role in their nanostructures. Among different nanocomposites, the CeO_2/FeO_x@mC_{500} displays highly graphitized mesoporous carbon structure, rich chemical functional groups, and homogeneous distribution of nanoparticles further leading to large amounts of antibody immobilization and sensitive determination of target CA19-9. The fabricated CeO_2/FeO_x@mC_{500}-based electrochemical immunosensor showed low LOD, excellent selectivity, good reproducibility, together with favorable stability and regenerability. And it also can be used in the detection of CA19-9 in human serum samples diluted 100-fold with 0.01 M PBS solution (pH 7.4) and spiked with different amounts of CA 19–9. Although this kind of new platform for detecting cancer marker was synthesized by the fussy method, the present work broaden the application range of MOFs and supply a potential for early diagnosis of cancer markers.

Declaration of interests

The authors declare that they have no known competing financial interests or personal relationships that could have appeared to influence the work reported in this paper.

CRediT authorship contribution statement

Minghua Wang: Validation, Formal analysis, Writing - original draft. **Mengyao Hu:** Methodology, Formal analysis, Investigation. **Bin Hu:** Methodology, Investigation. **Chuanpan Guo:** Visualization. **Yingpan Song:** Formal analysis. **Qiaojuan Jia:** Validation. **Linghao He:** Resources. **Zhihong Zhang:** Conceptualization, Writing - review & editing, Supervision. **Shaoming Fang:** Writing - review & editing.

Acknowledgements

We are grateful to the support from the National Natural Science Foundation of China (Nos. U1604127 and U1704256), Scientific and Technological Project of Henan Province (Nos.192102310261 and 192102310460), and Young Backbone Teacher Training Program in Universities of Henan Province (No. 2018GGJS089).

Appendix A. Supplementary data

Supplementary data to this article can be found online at https://doi.org/10.1016/j.bios.2019.04.018.

References

Alarfaj, A.N., El-Tohamy, F.M., Oraby, F.H., 2018. Int. J. Mol. Sci. 19 (4), 1162.
Bhardwaj, S.K., Sharma, A.L., Bhardwaj, N., Kukkar, M., Gill, A.A.S., Kim, K., Deep, A., 2017. Sensor. Actuator. B Chem. 240, 10–17.
Castillo-Blas, C., López-Salas, N., Gutiérrez, M.C., Puente-Orench, I., Gutiérrez-Puebla, E., Ferrer, M.L., Monge, M.Á., Gándara, F., 2019. J. Am. Chem. Soc. 141 (4), 1766–1774.
Cheng, N., Ren, L., Xu, X., Du, Y., Dou, S.X., 2018. Adv. Energy Mater. 8 (25), 1801257.
Ching, C.K., Rhodes, J.M., 1989. Br. J. Canc. 59, 949.
Dang, S., Zhu, Q., Xu, Q., 2017. Nat. Rev. Mater. 3, 17075.
Hidalgo, M., 2010. N. Engl. J. Med. 362 (17), 1605–1617.
Huang, Y., Wen, Y., Baryeh, K., Takalkar, S., Lund, M., Zhang, X., Liu, G., 2017. Microchim. Acta 184 (11), 4287–4294.
Humphris, J.L., Chang, D.K., Johns, A.L., Scarlett, C.J., Pajic, M., Jones, M.D., Colvin, E.K., Nagrial, A., Chin, V.T., Chantrill, L.A., Samra, J.S., Gill, A.J., Kench, J.G., Merrett, N.D., Das, A., Musgrove, E.A., Sutherland, R.L., Biankin, A.V., For, T.N.P.C., 2012. Ann. Oncol. 23 (7), 1713–1722.
Imaoka, H., Shimizu, Y., Senda, Y., Natsume, S., Mizuno, N., Hara, K., Hijioka, S., Hieda, N., Tajika, M., Tanaka, T., Ishihara, M., Niwa, Y., Yamao, K., 2016. Pancreatology 16 (4), 658–664.
Kašpar, J., Fornasiero, P., Graziani, M., 1999. Catal. Today 50 (2), 285–298.
Kumar, P., Kim, K., Bansal, V., Paul, A.K., Deep, A., 2016. Microchem. J. 128, 102–107.
Lei, J., Ju, H., 2012. Chem. Soc. Rev. 41 (6), 2122–2134.
Li, C., Heidt, D.G., Dalerba, P., Burant, C.F., Zhang, L., Adsay, V., Wicha, M., Clarke, M.F., Simeone, D.M., 2007. Cancer Res. 67 (3), 1030.
Li, G., Wang, X., Fu, J., Li, J., Park, M.G., Zhang, Y., Lui, G., Chen, Z., 2016. Angew. Chem. Int. Ed. 55 (16), 4977–4982.
Li, H., Wei, Y., Dong, X., Zang, S., Mak, T.C.W., 2015. Chem. Mater. 27 (4), 1327–1331.
Li, W., Li, L., Ge, S., Song, X., Ge, L., Yan, M., Yu, J., 2014. Biosens. Bioelectron. 56, 167–173.
Lin, J., Yan, F., Hu, X., Ju, H., 2004. J. Immunol. Methods 291 (1), 165–174.
Liu, C., Sun, C., Tian, J., Wang, Z., Ji, H., Song, Y., Zhang, S., Zhang, Z., He, L., Du, M., 2017a. Biosens. Bioelectron. 91, 804–810.
Liu, C., Zhang, Z., Chen, M., Zhao, H., Duan, F., Chen, D., Wang, M., Zhang, S., Du, M., 2017b. Chem. Commun. 53 (28), 3941–3944.
López-Alarcón, C., Denicola, A., 2013. Anal. Chim. Acta 763, 1–10.
Ludwig, J.A., Weinstein, J.N., 2005. Nat. Rev. Canc. 5, 845.
Lv, H., Zhang, H., Zhao, J., Ji, G., Du, Y., 2016. Nano Res 9 (6), 1813–1822.
Mai, H.D., Rafiq, K., Yoo, H., 2017. Chem. Eur J. 23 (24), 5631–5651.
Pachauri, N., Dave, K., Dinda, A., Solanki, P.R., 2018. J. Mater. Chem. B 6 (19), 3000–3012.
Pang, X., Li, J., Zhao, Y., Wu, D., Zhang, Y., Du, B., Ma, H., Wei, Q., 2015. ACS Appl. Mater. Interfaces 7 (34), 19260–19267.
Parker, N., Makin, C.A., Ching, C.K., Eccleston, D., Taylor, O.M., Milton, D., Rhodes, J.M., 1992. Cancer-Am. Cancer Soc. 70 (5), 1062–1068.
Peng, B., Cui, J., Wang, Y., Liu, J., Zheng, H., Jin, L., Zhang, X., Zhang, Y., Wu, Y., 2018. Nanoscale 10 (4), 1939–1945.
Sánchez, S., Roldán, M., Pérez, S., Fàbregas, E., 2008. Anal. Chem. 80 (17), 6508–6514.
Santharaman, P., Das, M., Singh, S.K., Sethy, N.K., Bhargava, K., Claussen, J.C., Karunakaran, C., 2016. Sensor. Actuator. B Chem. 236, 546–553.
Sha, Y., Guo, Z., Chen, B., Wang, S., Ge, G., Qiu, B., Jiang, X., 2015. Biosens. Bioelectron. 66, 468–473.
Sheikhzadeh, E., Chamsaz, M., Turner, A.P.F., Jager, E.W.H., Beni, V., 2016. Biosens. Bioelectron. 80, 194–200.
Shi, M., Zhao, S., Huang, Y., Zhao, L., Liu, Y., 2014. Talanta 124, 14–20.
Song, Y., Duan, F., Zhang, S., Tian, J., Zhang, Z., Wang, Z., Liu, C., Xu, W., Du, M., 2017. J. Mater. Chem. 5 (36), 19378–19389.
Tang, Z., He, J., Chen, J., Niu, Y., Zhao, Y., Zhang, Y., Yu, C., 2018. Biosens. Bioelectron. 101, 253–259.
Thapa, A., Soares, A.C., Soares, J.C., Awan, I.T., Volpati, D., Melendez, M.E., Fregnani, J.H.T.G., Carvalho, A.L., Oliveira, O.N., 2017. ACS Appl. Mater. Interfaces 9 (31), 25878–25886.
Wang, C., Wang, L., Tadepalli, S., Morrissey, J.J., Kharasch, E.D., Naik, R.R., Singamaneni, S., 2018a. ACS Sens. 3 (2), 342–351.
Wang, H., 2017. Coord. Chem. Rev. 349, 139–155.
Wang, M., Yang, L., Hu, B., Liu, J., He, L., Jia, Q., Song, Y., Zhang, Z., 2018b. Biosens. Bioelectron. 113, 16–24.
Wang, S., Li, Z., Duan, F., Hu, B., He, L., Wang, M., Zhou, N., Jia, Q., Zhang, Z., 2019. Anal. Chim. Acta 1047, 150–162.
Wang, Z., Dai, Z., 2015. Nanoscale 7 (15), 6420–6431.
Wei, W., Dong, S., Huang, G., Xie, Q., Huang, T., 2018. Sensor. Actuator. B Chem. 260, 189–197.
Weng, X., Liu, Y., Xue, Y., Wang, A., Wu, L., Feng, J., 2017. Sensor. Actuator. B Chem. 250, 61–68.
Xu, H., Shi, Z., Tong, Y., Li, G., 2018b. Adv. Mater. 30 (21), 1705442.
Xu, W., Qin, Z., Hao, Y., He, Q., Chen, S., Zhang, Z., Peng, D., Wen, H., Chen, J., Qiu, J., Li, C., 2018a. Biosens. Bioelectron. 113, 148–156.
Yang, F., Yang, Z., Zhuo, Y., Chai, Y., Yuan, R., 2015. Biosens. Bioelectron. 66, 356–362.
Yang, H., Wang, X., 2018. Adv. Mater. 0 (0), 1800743.
Yang, K., Yan, Y., Wang, H., Sun, Z., Chen, W., Kang, H., Han, Y., Zahng, W., Sun, X., Li, Z., 2018. Nanoscale 10 (37), 17647–17655.
Yang, L., Zhu, W., Ren, X., Khan, M.S., Zhang, Y., Du, B., Wei, Q., 2017a. Biosens. Bioelectron. 91, 842–848.
Yang, Z., Ren, S., Zhuo, Y., Yuan, R., Chai, Y., 2017b. Anal. Chem. 89 (24), 13349–13356.
Yu, H., Han, J., An, S., Xie, G., Chen, S., 2018. Biosens. Bioelectron. 109, 63–69.
Zhang, A., Xiang, H., Zhang, X., Guo, W., Yuan, E., Huang, C., Jia, N., 2016b. Biosens. Bioelectron. 75, 206–212.
Zhang, E., Xie, Y., Ci, S., Jia, J., Wen, Z., 2016a. Biosens. Bioelectron. 81, 46–53.
Zhang, F., Wang, P., Koberstein, J., Khalid, S., Chan, S., 2004. Surf. Sci. 563 (1), 74–82.
Zhang, T., Chang, H., Li, K., Peng, Y., Li, X., Li, J., 2018. Chem. Eng. J. 349, 184–191.
Zhang, X., Ke, H., Wang, Z., Guo, W., Zhang, A., Huang, C., Jia, N., 2017b. Analyst 142 (12), 2253–2260.
Zhang, Z., Ji, H., Song, Y., Zhang, S., Wang, M., Jia, C., Tian, J., He, L., Zhang, X., Liu, C., 2017a. Biosens. Bioelectron. 94, 358–364.
Zhao, Y., Wang, Q., Li, J., Ma, H., Zhang, Y., Wu, D., Du, B., Wei, Q., 2016. J. Mater. Chem. B 4 (17), 2963–2971.
Zhou, H.J., Kitagawa, S., 2014. Chem. Soc. Rev. 43 (16), 5415–5418.
Zhu, H., Fan, G., Abdel-Halim, E.S., Zhang, J., Zhu, J., 2016. Biosens. Bioelectron. 77, 339–346.
Zou, K., Li, Z., 2018. Chem. Eur J. 24 (25), 6506–6518.